

Article

An Investigation into the Effect of Length Scale of Reinforcement on the Cryogenic Response of a Mg/2wt.%CeO₂ Composite

Shwetabh Gupta ^{*,†} , Michael Johanes , Gururaj Parande  and Manoj Gupta ^{*} 

Department of Mechanical Engineering, National University of Singapore, 9 Engineering Drive 1, Singapore 117575, Singapore; michael.johanes@u.nus.edu (M.J.)

* Correspondence: shwetabh.gupta20@imperial.ac.uk (S.G.); mpegm@nus.edu.sg (M.G.);
Tel.: +65-6516-6358 (M.G.)

[†] Current address: Blakett Laboratory, Imperial College, London SW7 2AZ, UK.

Abstract: The present study attempted for the first time an investigation on the effect of deep cryogenic treatment in liquid nitrogen (LN) on magnesium–cerium oxide (Mg/2wt.%CeO₂) composites containing equal amounts of different length scales (micron and nanosize) cerium oxide (CeO₂) particles. The disintegrated melt deposition method was used to synthesize Mg-2CeO₂ micro- and nanocomposites, followed by hot extrusion as the secondary processing. Further liquid nitrogen treatment was performed at a cryogenic temperature of −196 °C. The combined effects of cryogenic treatment and reinforcement length scale on physical, mechanical, and thermal behaviors were studied. The results indicate that LN-treated micro- and nanocomposite samples exhibit, in common, a reduction in porosity, similar grain size, and a limited effect on the original texture of the matrix. However, microhardness, 0.2% Compressive Yield Strength (CYS), failure strain, and energy absorbed increased for both micro- and nanocomposite samples. Overall, results clearly indicate the capability of deep cryogenic treatment with LN to positively diversify the properties of both micro- and nanocomposite samples.

Keywords: magnesium; nanocomposite; cryogenic treatment; mechanical properties; ignition temperature; grain size



Citation: Gupta, S.; Johanes, M.; Parande, G.; Gupta, M. An Investigation into the Effect of Length Scale of Reinforcement on the Cryogenic Response of a Mg/2wt.%CeO₂ Composite. *Micro* **2024**, *4*, 170–184. <https://doi.org/10.3390/micro4010012>

Academic Editor: Ewa Kowalska

Received: 30 January 2024

Revised: 7 March 2024

Accepted: 12 March 2024

Published: 14 March 2024



Copyright: © 2024 by the authors. Licensee MDPI, Basel, Switzerland. This article is an open access article distributed under the terms and conditions of the Creative Commons Attribution (CC BY) license (<https://creativecommons.org/licenses/by/4.0/>).

1. Introduction

The commercial use of magnesium (Mg) and Mg-based materials is inevitable due to their attractive density (1.74 g/cm³), high specific strength, excellent electromagnetic shielding, easy availability, superior biocompatibility, and superior machineability [1–4]. This makes magnesium-based materials extremely suitable for both engineering and biomedical applications [5]. In engineering applications such as transportation (land, air, marine, and space), defense, sports, electronics, and robotics sectors, magnesium-based materials can play a key role in reducing energy consumption through lightweighting, while in the biomedical sector, they can serve as a bioresorbable temporary implant that will eliminate revision surgery and reduce patient trauma, medical costs, and burden on hospital facilities [6]. Although magnesium materials exhibit superior promise for use in various commercial sectors, their application is limited owing to shortcomings such as low fracture strain, ignition resistance, and expedited degradation in saline environments [7]. From a mechanical property standpoint, the key limitation of Mg-based materials is the limited range of mechanical properties when compared to the incumbent material of choice, Al-based alloys, which are almost 33% denser compared to Mg-based alloys. Researchers in the lightweight metal community have been working actively over the last 20 years to improve the property spans by (a) developing novel magnesium-based materials using alloying, composite, and multicomponent approaches, (b) innovating novel processing techniques to enhance the properties, and (c) using thermal treatment to tailor the properties as per the application requirement. Reasonable success has been achieved using all

three approaches; however, the understanding of the behavior of Mg-based materials can be further explored as the available information is limited. Hence, there is tremendous room to try new approaches to enhance the properties of Mg-based materials.

The use of composite technology has shown tremendous advancements in the past five decades, with fundamental research focused on aluminum-based microcomposites. Research on nanocomposites picked up in the late 1990s, with the focus gradually tilting toward magnesium-based nanocomposites. Both of these two types of composites (micro and nano) have certain advantages of their own; however, holistically, nanocomposites appear to have an edge over microcomposites, especially for magnesium. Mg-based nanocomposites, depending on judicious selection of reinforcement, have displayed superior hardness, tensile strength, compressive strength, creep resistance, tribological response, dry and wet corrosion resistance, and fatigue response, making them suitable for scale-up for industrial applications [8–11]. In order to further widen the spectrum of properties of magnesium-based composites, additional methods can be utilized, and these include the following: (a) judicious selection of primary and secondary processing techniques, (b) judicious matrix and reinforcement selection based on their compatibility, and (c) heat/cryogenic treatment, among others.

A possible composite material is CeO₂ (ceria), which possesses several attractive properties such as high hardness (6–8 on the Moh's scale) [12,13], wear resistance [14], corrosion resistance [15], good thermal stability [16,17], high specific chemical reactivity [18], as well as a high light refractive index and UV-absorption capability [19]. By virtue of this, it has found uses ranging from additives in ceramics [20], anti-corrosion coatings for metals [15], catalytic processes [17], electrochemicals [21], and solid oxide fuel cells [22], as well as thermal barriers and safeguards [18].

However, very limited work on the use of cryogenic treatment to influence the properties of Mg-based alloys is available in the literature [23,24]. Further, limited work has been published on Mg-based composites [25,26]. Gupta et al. [25] investigated the effect of liquid nitrogen exposure (−196 °C) on the mechanical properties of Mg-2CeO₂ nanocomposites. Exposure to liquid nitrogen leads to refined grain size, reduced porosity, and improved strength properties. Further, Gupta et al. [26] compared the effects of shallow and deep cryogenic treatments on the properties of Mg-CeO₂ nanocomposites. Deep cryogenically treated samples displayed an overall advantage in terms of mechanical properties and ignition temperature when compared to the shallow cryogenic treatment. A further literature search indicates that no work is performed on Mg-composites containing micron-size particle reinforcement.

Accordingly, the present study investigates the effect of deep cryogenic treatment (exposure to liquid nitrogen) on the physical, microstructural, and mechanical properties of Mg/2wt.%CeO₂ composites where CeO₂ reinforcement was used in both micron and nanolength scales and in the same amount. The emphasis is particularly placed on studying the effect of different length scales of reinforcement on the end properties of composites. The results are interesting and capable of developing a new research direction in the development of composite materials with better properties.

2. Materials and Methods

2.1. Materials

Magnesium (Mg) and cerium oxide (CeO₂) were used as matrix and reinforcement, respectively. The size of reinforcement, source, and purity of materials are listed in Table 1. Composites were made using 2wt.%CeO₂ particles on micron and nanolength scales.

Table 1. Materials used in the present study.

Raw Material	Size	Purity	Supplier
Magnesium	-	≥99.9%	Acros Organics, Morris Plains, NJ, USA
Cerium oxide (nanoscale)	15–30 nm	99.9%	Alfa Aesar GmbH & Co.
Cerium oxide (microscale)	5 μm	99.9%	KG, Haverhill, MA, USA

2.2. Processing

Composite materials were synthesized using the environment-friendly and flux-less disintegrated melt deposition (DMD) method. The procedure involved superheating the Mg turnings and CeO₂ particles placed in an alternating arrangement within a graphite crucible to a target superheat temperature of 750 °C, with argon used as the protective gas. The melt was stirred for 150 s using a mild steel impeller blade to ensure uniform distribution of the reinforcement and temperature homogenization of the Mg melt. The composite slurry was bottom-poured and subsequently disintegrated using argon gas jets before solidification into a solid cylindrical ingot. The ingots were then machined into billets with dimensions of 35.5 mm in diameter and 45 mm in length. Secondary processing followed, with first soaking at 400 °C for 60 min, followed by direct hot extrusion at 350 °C using a die with a diameter of 8 mm (extrusion ratio of 20.25:1), resulting in cylindrical extrudates.

The composites are then studied in 2 conditions: as-extruded (without further treatment, AE) and after exposure to liquid nitrogen for 24 h (LN). The temperature–time cycle for deep cryogenic treatment of LN samples is presented in Figure 1. Previous findings and recommendations were reviewed from the open literature to determine the exposure time at sub-zero temperatures [23,27].

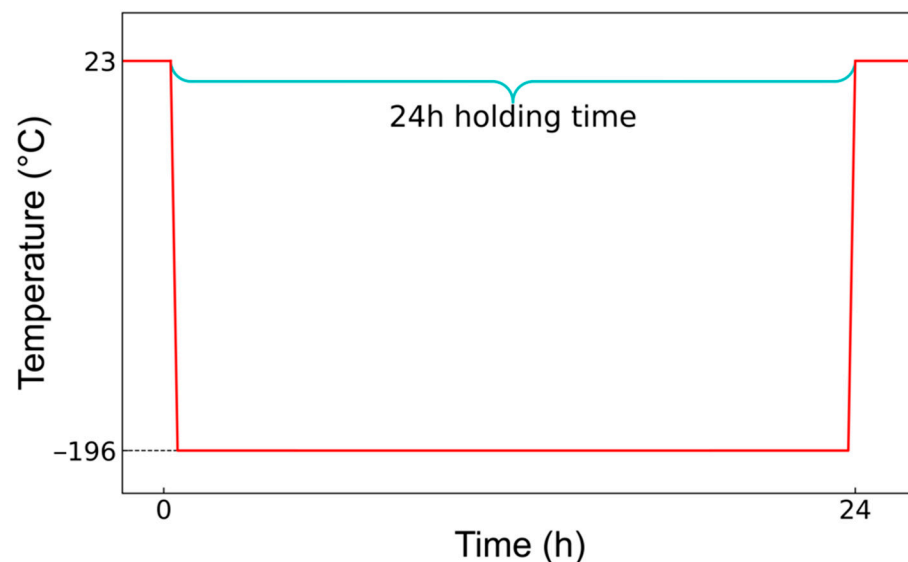


Figure 1. Temperature time cycle for LN materials in this work.

2.3. Characterization

2.3.1. Density and Porosity

The experimental densities of the samples before and after cryogenic treatment were determined using Archimedes' principle using an A&D GH-252 (AND Company, Limited, Tokyo, Japan) electronic scale, with five representative samples measured. The rule of mixtures was used to calculate the theoretical density of the Mg-2CeO₂ composite using the known constituent densities of Mg (1.738 g·cm⁻³) and CeO₂ (7.132 g·cm⁻³). Porosity was derived by comparing the measured experimental density against the calculated theoretical density.

2.3.2. Microstructure

Samples were ground and fine-finished using a 0.05 µm alumina suspension, followed by etching to reveal the grain boundaries. The nanosamples were etched using 10% oxalic acid with 3 drops of ethylene glycol, and the microsamples were etched using 5% citric acid with 3 drops of ethylene glycol. Using a Leica DM2500 optical microscope (Leica Microsystems (SEA) Pte Ltd., Singapore) and a JEOL JSM-6010 Scanning Electron Microscope (SEM, JEOL USA Inc., Peabody, MA, USA), representative grain images were

obtained. The images were analyzed for grain size and aspect ratio using MATLAB (version R2013b) based on a minimum of 6 vertices of each detected grain.

X-ray diffraction (XRD) studies were performed on the longitudinal surface of the material using a Shimadzu LAB-XRD-6000 (Shimadzu Corporation, Kyoto, Japan) automated spectrometer with Cu K_{α} radiation of 0.154056 nm wavelength, a scan range of 2θ between 20° and 75° , and a scan speed of $2^{\circ} \text{ min}^{-1}$, where θ is the Bragg angle.

2.3.3. Thermal Properties

A Differential Scanning Calorimetry (DSC) analysis was conducted using a Shimadzu DSC-60 (Shimadzu Corporation, Kyoto, Japan) and a temperature range of 30°C – 600°C , with a heating rate of $5^{\circ}\text{C}\cdot\text{min}^{-1}$ with argon gas supplied at $25 \text{ mL}\cdot\text{min}^{-1}$. This was performed to measure the effect of cryogenic treatment on the thermal response of the microstructural evolution of the material.

Ignition temperatures of Mg-2CeO₂ composites before and after the cryogenic treatments were determined using a Shimadzu DTG-60H Thermo Gravimetric Analyzer (Shimadzu Corporation, Kyoto, Japan). Parameters included a heating rate of $10^{\circ}\text{C} \text{ min}^{-1}$, purified air supply at $50 \text{ mL}\cdot\text{min}^{-1}$, and a measured temperature range of 30°C – 1000°C .

2.3.4. Mechanical Properties

Microhardness was measured using a Shimadzu HMV-2 automatic Vickers microhardness tester (Shimadzu Corporation, Kyoto, Japan) in accordance with ASTM standard E384-08 [28]. Indentations were performed with a 25 g force load and a dwell time of 15 s. A total of 20 representative readings were taken per sample.

A MTS E44 (MTS Systems, Eden Prairie, MN, USA) servohydraulic mechanical tester was used to conduct quasi-static compression of samples in accordance with procedures prescribed in standard ASTM E9-09 [29] at a strain rate of $5 \times 10^{-3} \text{ min}^{-1}$. Samples with a length-to-diameter (L/D) ratio of 1 were used, with a minimum of three representative compressions conducted. Post-fracture, compressive fractography was conducted, and the fracture images were studied to investigate the material's fracture response.

3. Results and Discussion

3.1. Density and Porosity

The results in Table 2 show that the deep cryogenic treatment (DCT) in liquid nitrogen reduced the porosity in both the micro- and nanocomposites. The percentage reduction in porosity was noticed to be higher in the nanocomposite samples in comparison to the microcomposite samples. The reduction in porosity can be in general attributed to (a) the development of compressive stresses [23,27] during the DCT that allowed the inward movement of the matrix in pores and (b) the capability of pores to serve as sinks for the extra dislocations that are generated during DCT treatment [30], which is enhanced for composites where the matrix and reinforcements have different coefficients of thermal expansion. Comparing the overall porosities, the microcomposite samples displayed lower porosities than the nanocomposite samples, both before and after the DCT.

Table 2. Results of density and porosity measurements.

Material	Before Treatment			After Treatment		
	Theoretical Density [g/cm ³]	Experimental Density [g/cm ³]	Porosity [%]	Experimental Density [g/cm ³]	Porosity [%]	Change in Porosity [%pt]
Pure Mg * [31]	1.7380	1.732 ± 0.0005	0.3190	-	-	-
Mg-2CeO ₂ (AE-nano) * [25,26]	1.7648	1.745 ± 0.002	1.099	-	-	-
Mg-2CeO ₂ (LN-nano) * [25,26]	1.7648	1.7476 ± 0.0009	0.9764	1.755 ± 0.002	0.5445	−0.4319 (↓44.2%)

Table 2. Cont.

Material	Before Treatment			After Treatment		Change in Porosity [%pt]
	Theoretical Density [g/cm ³]	Experimental Density [g/cm ³]	Porosity [%]	Experimental Density [g/cm ³]	Porosity [%]	
Mg-2CeO ₂ (AE-micron)	1.7648	1.760 ± 0.001	0.355	-	-	-
Mg-2CeO ₂ (LN-micron)	1.7648	1.7596 ± 0.002	0.2924	1.761 ± 0.001	0.2153	-0.0771 (↓26.3%)

*—Values obtained from other work using similar raw materials and processing methods. Downward arrows indicate decrease in property after treatment.

3.2. Microstructure

The results of the grain size measurements can be interpreted in two ways. The presence of the CeO₂ reinforcement in both the micron and nanolength scales reduces the grain size to approximately 1/10th of pure magnesium’s grain size (Table 3 and Figure 2). The average grain size of the nanocomposite samples remained approximately 31% lower than that of the microcomposite samples before cryogenic treatment. This can be attributed to the capability of a higher number of reinforcement particles to pin the movement of grain boundaries, and this is in line with the Zener relation, which states that the grain size of a given metal matrix decreases with the size of reinforcement particles [32,33]. Following the DCT, the grain size of the nanocomposite increased from 2 μm to 2.8 μm, but the microcomposite grain sizes remained unchanged. Furthermore, no conclusions can be drawn on the action of the DCT or the different length scales of the reinforcement on the aspect ratio of grains, as the values remained within each other’s standard deviations.

Table 3. Results of grain size measurements.

Composition	Mean Grain Size (μm)	Mean Aspect Ratio
Pure Mg [31]	21 ± 0.8	1.4 ± 0.2
Mg-2CeO ₂ (AE-nano) [25,26]	2 ± 0.6	1.4 ± 0.3
Mg-2CeO ₂ (LN-nano) [25,26]	2.8 ± 0.6	1.2 ± 0.3
Mg-2CeO ₂ (AE-micron)	2.9 ± 0.8	1.5 ± 0.3
Mg-2CeO ₂ (LN-micron)	2.8 ± 0.8	1.6 ± 0.5

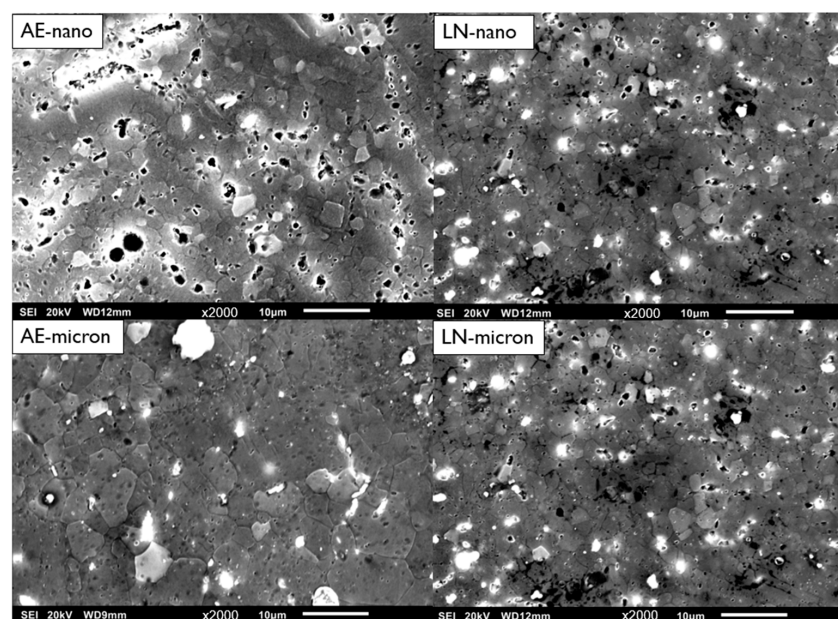


Figure 2. Grain microstructure of Mg-2CeO₂ materials in this work.

The results of XRD studies are detailed in Table 4 and Figure 3. The results revealed that the nanocomposite samples displayed a dominant basal texture both before and after cryogenic treatment. The basal texture became stronger after the DCT, as evidenced by the reduction in the relative intensities of the prismatic and pyramidal planes. In the microcomposite samples, the dominant texture was pyramidal both before and after DCT. The pyramidal texture became stronger upon the DCT as the relative intensities of the prismatic and basal planes were reduced. These results both show that the DCT assisted in strengthening the texture of the as-extruded samples but was not capable of randomizing the texture. Therefore, the XRD results clearly reveal that the length scale of the reinforcement affects the textural development of the matrix and that the DCT strengthens the prevailing texture (basal or pyramidal) of the as-extruded samples. The end properties of the different composites can hence be expected to be different for both as-extruded and after DCT.

Table 4. Relative intensities of Mg crystalline plane peaks.

Material	Plane	I/I_{\max}
Mg-2CeO ₂ (AE-nano) [25,26]	10–10 prism	0.217021
	0002 basal	1
	10–11 pyramidal	0.753191
Mg-2CeO ₂ (LN-nano) [25,26]	10–10 prism	0.104399
	0002 basal	1
	10–11 pyramidal	0.52514
Mg-2CeO ₂ (AE-micron)	10–10 prism	0.21600
	0002 basal	0.75415
	10–11 pyramidal	1
Mg-2CeO ₂ (LN-micron)	10–10 prism	0.21109
	0002 basal	0.40639
	10–11 pyramidal	1

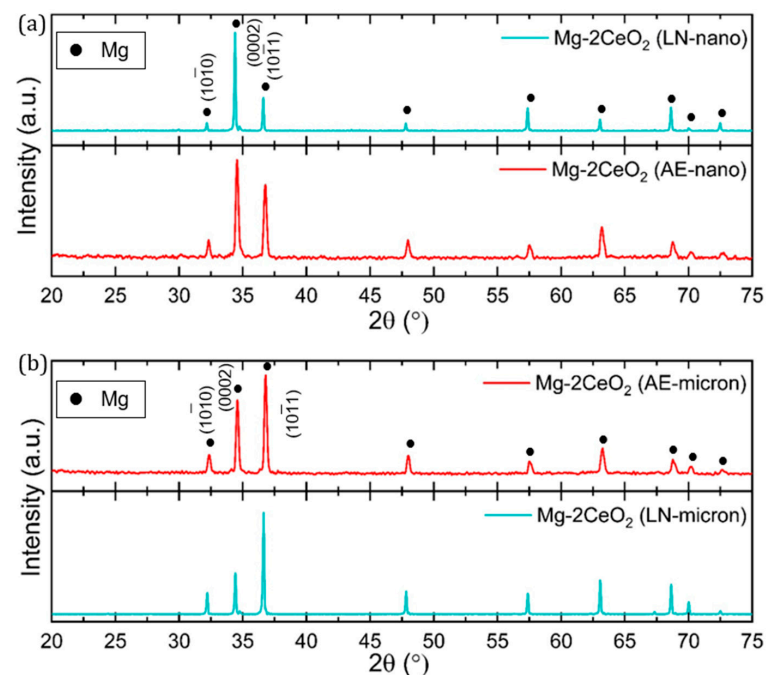


Figure 3. X-ray diffractogram for (a) Mg-2CeO₂ nanocomposite and (b) Mg-2CeO₂ microcomposite.

3.3. Thermal Response

The results of the DSC studies are plotted in Figure 4. As no alloying element was used in the magnesium matrix (>99.9% pure), dissolution or precipitation of secondary phases was ruled out. Minor exothermic peaks were observed in liquid nitrogen-treated micro- and nanocomposite samples at ~484 °C and 469 °C, respectively. These peaks can be attributed to the release of compressive stresses stored during DCT within the matrix and particle–matrix interfaces. The results are consistent with earlier findings [25,26].

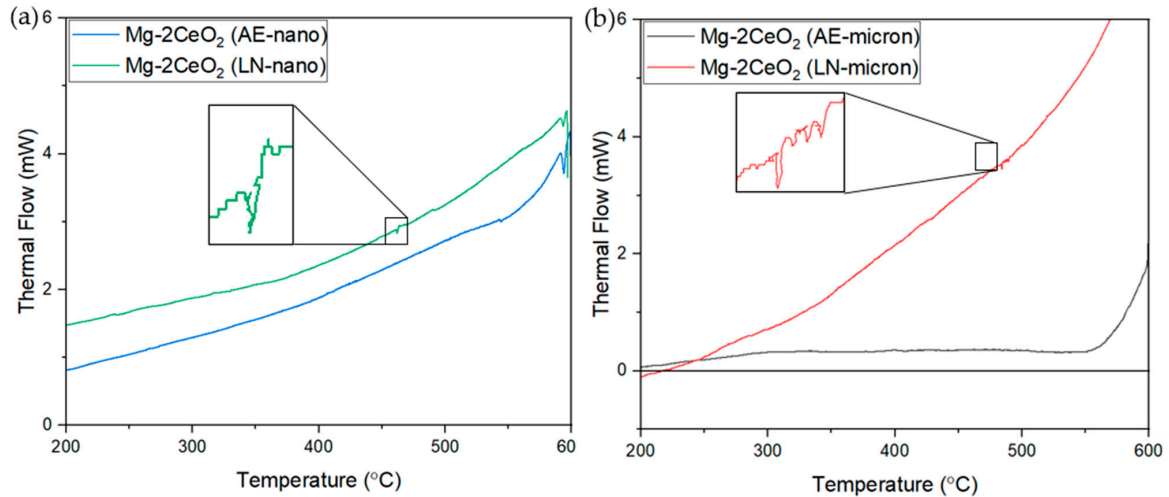


Figure 4. Results of DSC studies for (a) Mg-2CeO₂ nanocomposite and (b) Mg-2CeO₂ microcomposite.

The ignition studies reveal that the presence of reinforcement in micron and nano-length scales increased the ignition temperature by 11.0% (64 °C) and 10.0% (58 °C), respectively, when compared to pure magnesium in the as-extruded condition (Table 5 and Figure 5). The results are consistent with observations made by researchers earlier, which attributed a direct relationship between a decrease in thermal conductivity (owing to the presence of reinforcement) and an increase in ignition temperature [34,35]. As the thermal conductivity of the materials is affected by the amount of porosity [36] and grain size [37], the lower grain sizes (Table 3) and higher porosities (Table 2) of the as-extruded composites compared to pure magnesium are likely contributors to their higher ignition temperatures.

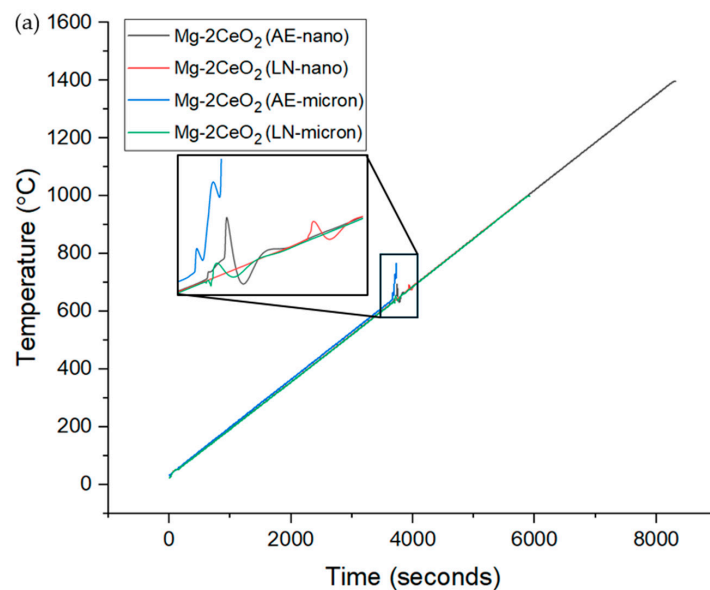


Figure 5. Cont.

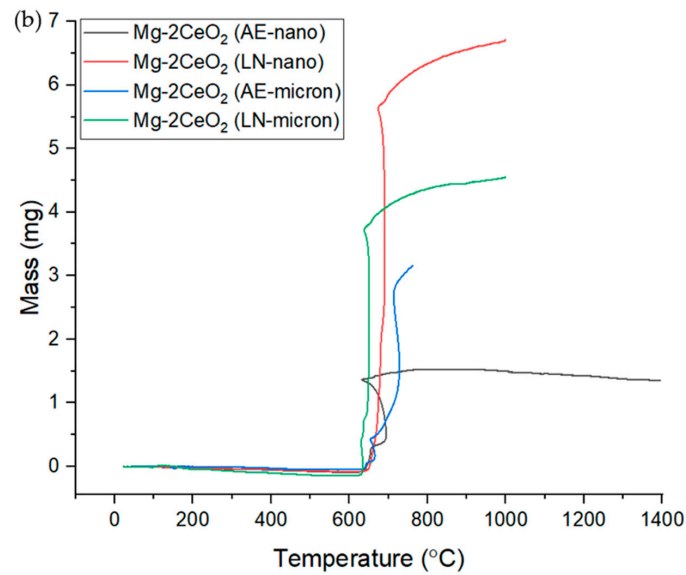


Figure 5. Thermogravimetric plots of Mg-2CeO₂ materials in this work in (a) time vs. temperature and (b) mass vs. temperature form.

Following the DCT, the thermal conductivities of the micro- and nanocomposite samples will be dependent on the remaining porosity and dislocation density, as their average grain sizes are similar. Considering the larger number of reinforcement particles in the matrix for nanocomposites (the ratio of the number of particles on the nanolength scale and the micron length scale $\approx n_{\text{nano}}/n_{\text{micron}} = 4.6 \times 10^6$), their capability to increase the dislocation density will be higher. This is evident by the larger increase in their hardness value (Table 6). This capability of dislocations to scatter phonons and, thus, reduce thermal conductivity is well established [38]. Expectedly, the ignition temperature of Mg-2CeO₂ (LN-nano) remained 36 °C higher when compared to Mg-2CeO₂ (LN-micron).

Table 5. Results of ignition temperature measurements.

Composition	Ignition Temperature (°C)
Pure Mg	580
Mg-2CeO ₂ (AE-nano)	638 (↑10.0%)
Mg-2CeO ₂ (LN-nano)	676 (↑16.6%)
Mg-2CeO ₂ (AE-micron)	644 (↑11.0%)
Mg-2CeO ₂ (LN-micron)	637 (↑9.8%)
AZ31 [39]	628
AZ61 [40]	559
AZ81A [40]	543
AZ91 [39,40]	600
ZK40A [40]	500
ZK60A [40]	499
AM50 [40]	585
WE43 [40,41]	644

↑—The increase indicated is with respect to pure Mg.

Table 6. Results of hardness measurements.

Composition	Microhardness (HV)
Pure Mg [31]	55 ± 3
Mg-2CeO ₂ (AE-nano) [25]	86 ± 2
Mg-2CeO ₂ (LN-nano) [25,26]	92 ± 4 (↑7%)
Mg-2CeO ₂ (AE-micron)	74 ± 3
Mg-2CeO ₂ (LN-micron)	88 ± 7 (↑19%)

↑—The increase is with respect to the respective as-extruded condition.

The results of the XRD texture analysis and ignition temperature measurements (Table 5) revealed the following:

- The samples exhibiting basal texture, Mg-2CeO₂ (AE-nano) and Mg-2CeO₂ (LN-nano), showed higher ignition temperatures than the Mg-2CeO₂ (AE-micron) and Mg-2CeO₂ (LN-micron) samples showing pyramidal texture.
- Within the Mg-2CeO₂ nanocomposites, the weakened basal texture in Mg-2CeO₂ (AE-nano), as evidenced by the intensities of prismatic and pyramidal peaks, leads to a reduced ignition temperature.
- Within the Mg-2CeO₂ microcomposites, the weakened pyramidal texture in Mg-2CeO₂ (AE) increases the ignition temperature. In this case, the basal peak was stronger (Figure 2).

The results of this study directly indicate that an increase in the basal texture in the case of magnesium-based nanocomposites has a strong and direct positive correlation with the ignition temperature. The present study also showcases the superiority of both micro- and nanocomposites, in the context of ignition temperature, to commercial magnesium-based alloys such as the AZ and ZK series and the WE 43 alloys (Table 5).

3.4. Mechanical Response

The mechanical response of the samples was assessed in the context of hardness (microhardness) and compressive response (CYS, UCS, and fracture strain). The results of the hardness measurements (Table 6) reveal that the hardness of composite samples with or without cryogenic treatment was superior when compared to pure Mg. This can be attributed to (a) the presence of harder ceramic particles (Moh's hardness of CeO₂ and Mg being 6–8 [12,13] and 2 [2], respectively), (b) a reduction in grain size (Table 3) in line with the Hall–Patch relationship [42–44], and (c) an increase in the dislocation density in the matrix due to CTE differences between metallic Mg and ceramic CeO₂.

The DCT-treated samples exhibited an increase in hardness in composite samples, within both length scales (micro and nano). The results are consistent with the capability of DCT to (a) further increase the dislocation density [23,30,45], (b) decrease the porosity (Table 2), and (c) strain the lattice due to induced compressive stresses [23,30,45]. Comparing the length scales of the reinforcement, the composites with micron length scale reinforcements showed lower hardness when compared to those with nanolength scale reinforcements in both AE and LN conditions. This can be attributed to the larger number of nanolength scale particles (reduced particle-free matrix zones) and, accordingly, their capability to resist the localized deformation more effectively.

The compressive response of the samples (Figure 6) in the context of the presence and length scale of reinforcements and DCT is described succinctly in the subsequent paragraphs. The presence of the CeO₂ reinforcement in either length scale increased the 0.2 CYS and UCS of the Mg matrix. The fracture strain remained higher for the Mg-CeO₂ (LN-nano) and Mg-CeO₂ (AE-micron and LN-micron) samples. The increase in strengths in the case of the composite samples can be attributed to particle-associated strengthening mechanisms such as grain size strengthening and dislocation density-related strengthening that originate due to CTE and elastic modulus mismatch [46]. The increase

in the fracture strain of the Mg-2 CeO₂ (LN-nano) samples can be attributed to an increase in interfacial bonding during the LN treatment (due to compressive stresses), delaying both crack initiation and crack propagation [25]. The higher fracture strain of the Mg-2 CeO₂ microcomposites before and after LN treatment compared to the nanocomposites can be attributed to the dominating pyramidal texture rather than the basal texture [47].

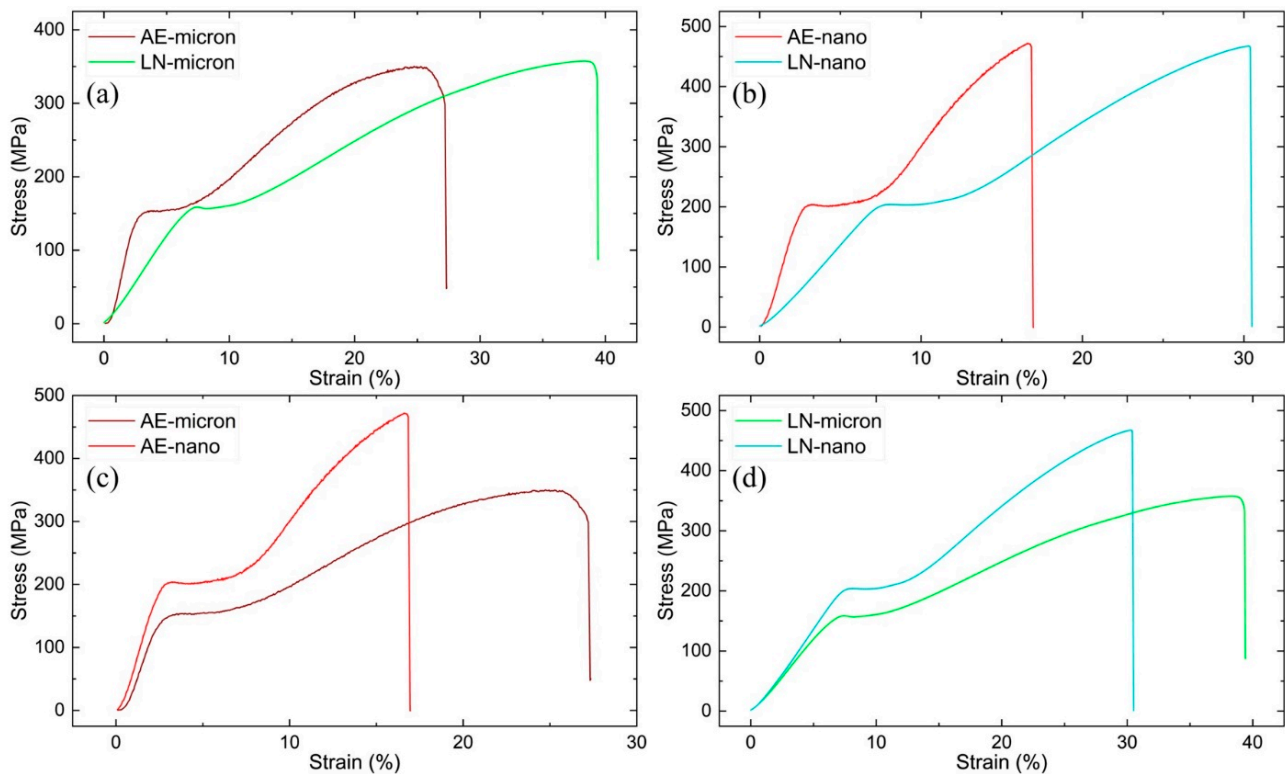


Figure 6. Compressive stress–strain diagrams of materials in this work, grouped into (a) microcomposites, (b) nanocomposites, (c) as-extruded materials, and (d) LN-treated materials.

Results show that LN treatment in both types of composites leads to an increase in the 0.2 CYS and fracture strain (Table 7, Figure 6a,b). The grain size effect is ruled out as the grain sizes of all the samples are very similar and within each other's standard deviation (Table 3). The increase in 0.2 CYS following LN treatment and a significant reduction in its standard deviation indicate homogenization of the matrix microstructure, more predictable deformation, and an increase in the stresses required to initiate the motion of dislocations, which is characteristic of the yield point and yield zone. No trend was observed in the UCS values, as they remained within each other's standard deviations. In both the micro- and nanosamples, the LN treatment led to an increase in failure strain, which can be attributed to an improvement in interfacial characteristics due to improved matrix-reinforcement bonding triggered through the LN treatment, as described elsewhere [6]. The nanocomposite samples displayed higher strength levels (0.2 CYS and UCS), while the microcomposite samples showed higher failure strain levels in both AE and LN conditions (Figure 6c,d). The relatively higher strength of the nanocomposite samples can primarily be attributed to the Orowan strengthening and higher basal texture [48], both of which are missing in the microcomposites. The higher failure strain of the microcomposites in both the AE and LN conditions (Figure 6a,b) can be attributed to their pyramidal texture [47].

Table 7. Results of compressive property measurements.

Composition	0.2 CYS (MPa)	UCS (MPa)	Total Fracture Strain (%)	Plastic Fracture Strain (%)	Energy Absorbed (MJ/m ³)
Pure Mg [31]	63 ± 4	278 ± 5	24 ± 1	-	45
Mg-2CeO ₂ (AE-nano) [26]	178 ± 19	473 ± 16	16.5 ± 0.7	10.5	43.3 ± 1.8
Mg-2CeO ₂ (LN-nano) [26]	203 ± 5 (↑14.2%)	452 ± 15 (↓4.4%)	29.7 ± 1.2 (↑80%)	13.0	76 ± 6 (↑72%)
Mg-2CeO ₂ (AE-micron)	142 ± 11	341 ± 8	29 ± 3	21.0	70 ± 10
Mg-2CeO ₂ (LN-micron)	157.5 ± 1 (↑10.9%)	347.6 ± 6 (↑1.9%)	37 ± 3 (↑27.6%)	23.0	100 ± 8 (↑42.9%)
AM50 [49]	110	312	11.5	-	
AZ91D [50]	130	300	12.4	-	
AZ31 [51]	-	250	28	-	
Mg-5Zn/5BG [26]	-	112.8	-	-	
WE43 [52]	261 ± 16	420 ± 13	16.3 ± 1.0	-	
WE43 + Apatite [52]	229 ± 6	380.1 ± 9.0	11.7 ± 0.5	-	NA
ME21 [53]	87	260	25	-	
WE54 [26]	210	325	27	-	
ZK60 [54]	159	472	12.4	-	
Mg ₄ Zn ₃ Gd ₁ Ca [26]	260 ± 3	585 ± 18	12.6 ± 0.3	-	
Mg ₄ Zn ₃ Gd ₁ Ca-ZnO [26]	355 ± 5	703 ± 40	10.6 ± 0.3	-	

Arrows indicate increase or decrease relative to as-extruded condition.

A visual examination of the fractographic studies conducted on the micro- and nanocomposite samples (Figure 7) indicates that the samples exhibited approximately 45° fractures with respect to the compression axis. No effect of LN treatment and length scale of reinforcement particles was thus observed at the macro level.

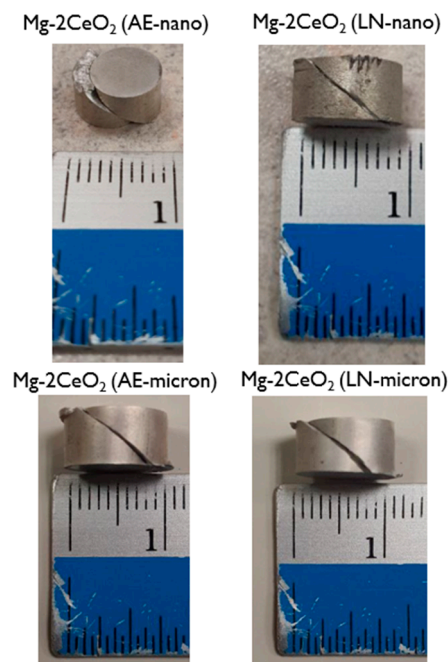


Figure 7. Macroscopic images of compressively fractured samples.

At the microscopic level, the fractographs of Mg-2CeO₂ (AE-micron) samples revealed relatively rougher surfaces indicative of more plastic deformation when compared to the Mg-2CeO₂ (AE-nano) samples (Figure 8). This indicates that Mg-2CeO₂ (AE-micron) samples have undergone more plastic deformation, which is also evident from their fracture strain (Table 7), where the microcomposites exhibit ~75% higher total fracture strain in the AE condition when compared to nanocomposites. For the LN-treated samples, the fractographs showed the presence of a limited number of microcracks in Mg-2CeO₂ (LN-nano), which were absent in Mg-2CeO₂ (LN-micron) samples (Figure 8). The presence of cracks may be attributed to the clustering points of nano-CeO₂ particles (often associated with voids), which cannot be avoided, particularly for nanolength scale reinforcements, irrespective of the processing method used (powder metallurgy or casting). The significantly higher fracture strain exhibited by Mg-2CeO₂ (LN-micron) composites (37%) when compared to Mg-2CeO₂ (LN-nano) composites (29.7%) can thus be attributed to the absence of microcrack development during compressive loading besides pyramidal texture.

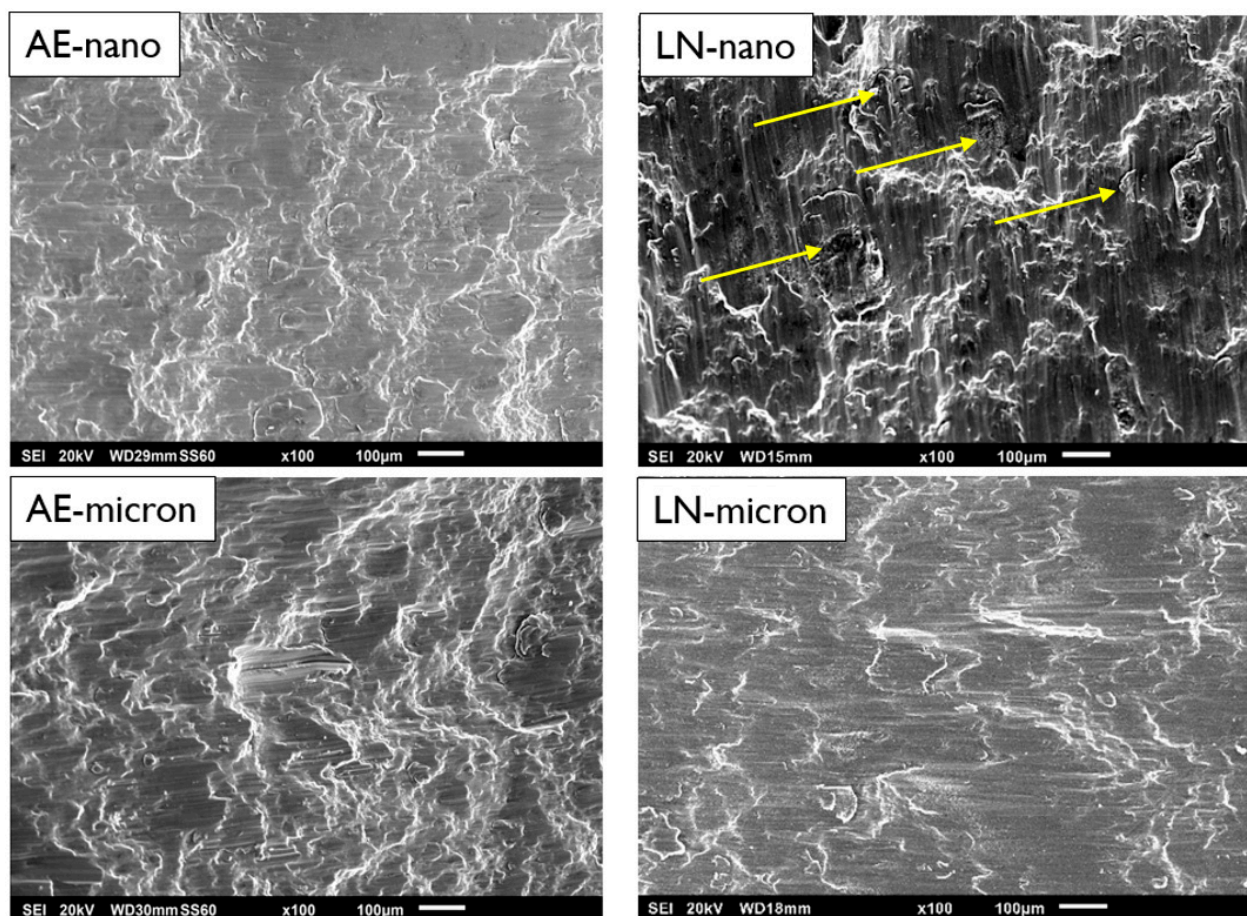


Figure 8. SEM micrographs of compressively fractured samples, with microcracks indicated by yellow arrows.

4. Conclusions

In this study, the combined effects of the deep cryogenic treatment and the length scale of the reinforcement on the properties of Mg-2CeO₂ composites were studied. The following observations were made:

- a. At a constant amount of CeO₂ (2wt.%), the grain sizes of the composite samples (micro- and nanocomposites) remained similar. Deep cryogenic treatment did not noticeably affect grain size at either length scale of reinforcement.

- b. The porosity values were reduced when the as-extruded micro- and nanocomposite samples were deep cryogenically treated (reduction of 0.08 and 0.43%pt, respectively).
- c. The deep cryogenic treatment did not randomize the texture of composites, which remained basal for nanocomposites and pyramidal for microcomposites. Instead, the intensity of individual peaks changed to further strengthen the original texture.
- d. The deep cryogenic treatment had a stronger effect on increasing ignition temperature in the case of the nanocomposite samples. This can be attributed to the coupled and complex effects of the number of particles in the matrix and the texture of the matrix.
- e. The deep cryogenic treatment enhanced the microhardness, 0.2 CYS, and fracture strain of both micro- and nanocomposite samples. The changes in UCS remained insignificant. The fracture strain increased significantly for nanocomposites (~80%) and microcomposites (27.6%).

Author Contributions: Conceptualization, S.G. and M.G.; methodology, S.G. and M.G.; software, S.G.; validation, S.G. and G.P.; formal analysis, S.G., M.J. and G.P.; investigation, S.G., M.J. and G.P.; resources, M.G.; data curation, S.G., M.J. and G.P.; writing—original draft preparation, S.G.; writing—review and editing, S.G., M.J., G.P. and M.G.; visualization, S.G. and M.J.; supervision, M.G.; project administration, M.G. All authors have read and agreed to the published version of the manuscript.

Funding: This research received no external funding.

Institutional Review Board Statement: Not applicable.

Informed Consent Statement: Not applicable.

Data Availability Statement: The original contributions presented in the study are included in the article, further inquiries can be directed to the corresponding author.

Acknowledgments: The authors would like to thank the experimental support extended by Khin Sandar Tun and Hong Wei from the Department of Mechanical Engineering, National University of Singapore.

Conflicts of Interest: The authors declare no conflicts of interest.

References

1. Charyeva, O.; Dakischew, O.; Sommer, U.; Heiss, C.; Schnettler, R.; Lips, K.S. Biocompatibility of magnesium implants in primary human reaming debris-derived cells stem cells in vitro. *J. Orthop. Traumatol.* **2016**, *17*, 63–73. [CrossRef] [PubMed]
2. Geoscience Australia. Magnesium. Available online: <https://www.ga.gov.au/education/minerals-energy/australian-mineral-facts/magnesium> (accessed on 23 February 2024).
3. Gupta, M.; Sharon, N.M.L. Chapter 4—Fundamentals of Metal Matrix Composites. In *Magnesium, Magnesium Alloys, and Magnesium Composites*; John Wiley & Sons: Hoboken, NJ, USA, 2010. [CrossRef]
4. Akyuz, B. Machinability of Magnesium and Its Alloys. *TOJSAT Online J. Sci. Technol.* **2011**, *1*, 31–38.
5. Maier, P.; Hort, N. Magnesium Alloys for Biomedical Applications. *Metals* **2020**, *10*, 1328. [CrossRef]
6. Prasad, S.; Raguraman, S.; Wong, R.; Gupta, M. Current Status and Outlook of Temporary Implants (Magnesium/Zinc) in Cardiovascular Applications. *Metals* **2022**, *12*, 999. [CrossRef]
7. Yu, Z.; Chen, J.; Yan, H.; Xia, W.; Su, B.; Gong, X.; Guo, H. Degradation, stress corrosion cracking behavior and cytocompatibility of high strain rate rolled Mg-Zn-Sr alloys. *Mater. Lett.* **2020**, *260*, 126920. [CrossRef]
8. Mishra, S.K.; Manakari, V.; Parande, G.; Matli, P.R.; Gupta, M. Development of Ultralight Binary Mg-Li Alloys: Enhancing Damping, Ductility, and Ultimate Compressive Strength beyond 2000 MPa. *J. Mater. Eng. Perform.* **2023**, *32*, 2723–2734. [CrossRef]
9. Bupesh Raja, V.K.; Parande, G.; Kannan, S.; Sonawwanay, P.D.; Selvarani, V.; Ramasubramanian, S.; Ramachandran, D.; Jeremiah, A.; Akash Sundaraeswar, K.; Satheshwaran, S.; et al. Influence of Laser Treatment Medium on the Surface Topography Characteristics of Laser Surface-Modified Resorbable Mg3Zn Alloy and Mg3Zn1HA Nanocomposite. *Metals* **2023**, *13*, 850. [CrossRef]
10. Guo, Y.C.; Nie, K.B.; Kang, X.K.; Deng, K.K.; Han, J.G.; Zhu, Z.H. Achieving high-strength magnesium matrix nanocomposite through synergistical effect of external hybrid (SiC+TiC) nanoparticles and dynamic precipitated phase. *J. Alloys Compd.* **2019**, *771*, 847–856. [CrossRef]
11. Kujur, M.S.; Manakari, V.; Parande, G.; Prasad, S.; Wong, R.; Mallick, A.; Gupta, M. Development of rare-earth oxide reinforced magnesium nanocomposites for orthopaedic applications: A mechanical/immersion/biocompatibility perspective. *J. Mech. Behav. Biomed. Mater.* **2021**, *114*, 104162. [CrossRef]

12. He, Q. Experimental study on polishing performance of CeO₂ and nano-SiO₂ mixed abrasive. *Appl. Nanosci.* **2018**, *8*, 163–171. [[CrossRef](#)]
13. Borra, C.R.; Vlugt, T.J.H.; Yang, Y.; Offerman, S.E. Recovery of Cerium from Glass Polishing Waste: A Critical Review. *Metals* **2018**, *8*, 801. [[CrossRef](#)]
14. Kabir, M.S.; Zhou, Z.; Xie, Z.; Munroe, P. Scratch and wear resistance of hydrophobic CeO_{2-x} coatings synthesized by reactive magnetron sputtering. *Ceram. Int.* **2020**, *46*, 89–97. [[CrossRef](#)]
15. Thiruvoth, D.D.; Ananthkumar, M. Evaluation of cerium oxide nanoparticle coating as corrosion inhibitor for mild steel. *Mater. Today Proc.* **2022**, *49*, 2007–2012. [[CrossRef](#)]
16. Eyring, L. Chapter 27: The binary rare earth oxides. In *Handbook on the Physics and Chemistry of Rare Earths*; Elsevier: Amsterdam, The Netherlands, 1979; Volume 3, pp. 337–399.
17. Trovarelli, A.; de Leitenburg, C.; Boaro, M.; Dolcetti, G. The utilization of ceria in industrial catalysis. *Catal. Today* **1999**, *50*, 353–367. [[CrossRef](#)]
18. Chen, H.-I.; Chang, H.-Y. Synthesis and characterization of nanocrystalline cerium oxide powders by two-stage non-isothermal precipitation. *Solid State Commun.* **2005**, *133*, 593–598. [[CrossRef](#)]
19. Tsunekawa, S.; Sahara, R.; Kawazoe, Y.; Kasuya, A. Origin of the Blue Shift in Ultraviolet Absorption Spectra of Nanocrystalline CeO_{2-x} Particles. *Mater. Trans. JIM* **2000**, *41*, 1104–1107. [[CrossRef](#)]
20. Lin, J.-D.; Duh, J.-G. Fracture toughness and hardness of ceria- and yttria-doped tetragonal zirconia ceramics. *Mater. Chem. Phys.* **2003**, *78*, 253–261. [[CrossRef](#)]
21. Castano, C.E.; O’Keefe, M.J.; Fahrenholtz, W.G. Cerium-based oxide coatings. *Curr. Opin. Solid State Mater. Sci.* **2015**, *19*, 69–76. [[CrossRef](#)]
22. Sun, C.; Li, H.; Chen, L. Nanostructured ceria-based materials: Synthesis, properties, and applications. *Energy Environ. Sci.* **2012**, *5*, 8475–8505. [[CrossRef](#)]
23. Sonar, T.; Lomte, S.; Gogte, C. Cryogenic Treatment of Metal—A Review. *Mater. Today Proc.* **2018**, *5*, 25219–25228. [[CrossRef](#)]
24. Dieringa, H. Influence of Cryogenic Temperatures on the Microstructure and Mechanical Properties of Magnesium Alloys: A Review. *Metals* **2017**, *7*, 38. [[CrossRef](#)]
25. Gupta, S.; Parande, G.; Tun, K.S.; Gupta, M. Enhancing the Physical, Thermal, and Mechanical Responses of a Mg/2wt.%CeO₂ Nanocomposite Using Deep Cryogenic Treatment. *Metals* **2023**, *13*, 660. [[CrossRef](#)]
26. Gupta, S.; Parande, G.; Gupta, M. Comparison of Shallow (−20 °C) and Deep Cryogenic Treatment (−196 °C) to Enhance the Properties of a Mg/2wt.%CeO₂ Nanocomposite. *Technologies* **2024**, *12*, 14. [[CrossRef](#)]
27. Baldiserra, P.; Delprete, C. Deep Cryogenic Treatment: A Bibliographic Review. *Open Mech. Eng. J.* **2008**, *2*, 1–11. [[CrossRef](#)]
28. ASTM E384-08; Standard Test Method for Microindentation Hardness of Materials. ASTM International: West Conshohocken, PA, USA, 2010. [[CrossRef](#)]
29. ASTM E9-09; Standard Test Methods of Compression Testing of Metallic Materials at Room Temperature. ASTM International: West Conshohocken, PA, USA, 2018. [[CrossRef](#)]
30. Huang, H.; Zhang, J. Microstructure and mechanical properties of AZ31 magnesium alloy processed by multi-directional forging at different temperatures. *Mater. Sci. Eng. A* **2016**, *674*, 52–58. [[CrossRef](#)]
31. Parande, G.; Tun, K.S.; Neo, H.J.N.; Gupta, M. An Investigation into the Effect of Length Scale (Nano to Micron) of Cerium Oxide Particles on the Mechanical and Flammability Response of Magnesium. *J. Mater. Eng. Perform.* **2023**, *32*, 2710–2722. [[CrossRef](#)]
32. Rohrer, G.S. “Introduction to Grains, Phases, and Interfaces—An Interpretation of Microstructure,” *Trans. AIME*, 1948, vol. 175, pp. 15–51, by C.S. Smith. *Metall. Mater. Trans. A* **2010**, *41*, 1063–1100. [[CrossRef](#)]
33. Smith, C.S. Grains, phases, and interphases: An interpretation of microstructure. *Trans. Metall. Soc. AIME* **1948**, *175*, 15–51.
34. Parande, G.; Manakari, V.; Meenashisundaram, G.K.; Gupta, M. Enhancing the tensile and ignition response of monolithic magnesium by reinforcing with silica nanoparticulates. *J. Mater. Res.* **2017**, *32*, 2169–2178. [[CrossRef](#)]
35. Manakari, V.; Parande, G.; Doddamani, M.; Gupta, M. Enhancing the Ignition, Hardness and Compressive Response of Magnesium by Reinforcing with Hollow Glass Microballoons. *Materials* **2017**, *10*, 997. [[CrossRef](#)]
36. Francl, J.; Kingery, W.D. Thermal Conductivity: IX, Experimental Investigation of Effect of Porosity on Thermal Conductivity. *J. Am. Ceram. Soc.* **1954**, *37*, 99–107. [[CrossRef](#)]
37. Sood, A.; Cheaito, R.; Bai, T.; Kwon, H.; Wang, Y.; Li, C.; Yates, L.; Bougher, T.; Graham, S.; Asheghi, M.; et al. Direct Visualization of Thermal Conductivity Suppression Due to Enhanced Phonon Scattering Near Individual Grain Boundaries. *Nano Lett.* **2018**, *18*, 3466–3472. [[CrossRef](#)]
38. Kogure, Y.; Hiki, Y. Effect of Dislocations on Low-Temperature Thermal Conductivity and Specific Heat of Copper-Aluminum Alloy Crystals. *J. Phys. Soc. Jpn.* **1975**, *39*, 698–707. [[CrossRef](#)]
39. Liu, M.; Shih, D.S.; Parish, C.; Atrens, A. The ignition temperature of Mg alloys WE43, AZ31 and AZ91. *Corros. Sci.* **2012**, *54*, 139–142. [[CrossRef](#)]
40. Tekumalla, S.; Gupta, M. An insight into ignition factors and mechanisms of magnesium based materials: A review. *Mater. Des.* **2017**, *113*, 84–98. [[CrossRef](#)]
41. Ravi Kumar, N.V.; Blandin, J.J.; Suéry, M.; Grosjean, E. Effect of alloying elements on the ignition resistance of magnesium alloys. *Scr. Mater.* **2003**, *49*, 225–230. [[CrossRef](#)]

42. Taha, A.S.; Hammad, F.H. Application of the Hall-Petch Relation to Microhardness Measurements on Al, Cu, Al-MD 105, and Al-Cu Alloys. *Phys. Status Solidi (A)* **1990**, *119*, 455–462. [[CrossRef](#)]
43. Yu, H.; Xin, Y.; Wang, M.; Liu, Q. Hall-Petch relationship in Mg alloys: A review. *J. Mater. Sci. Technol.* **2018**, *34*, 248–256. [[CrossRef](#)]
44. Wang, Y.; Choo, H. Influence of texture on Hall–Petch relationships in an Mg alloy. *Acta Mater.* **2014**, *81*, 83–97. [[CrossRef](#)]
45. Jiang, Y.; Chen, D.; Chen, Z.; Liu, J. Effect of Cryogenic Treatment on the Microstructure and Mechanical Properties of AZ31 Magnesium Alloy. *Mater. Manuf. Process.* **2010**, *25*, 837–841. [[CrossRef](#)]
46. Ibrahim, I.A.; Mohamed, F.A.; Lavernia, E.J. Particulate reinforced metal matrix composites—A review. *J. Mater. Sci.* **1991**, *26*, 1137–1156. [[CrossRef](#)]
47. Hamad, K. Highly-Ductile Magnesium Alloys: Atomistic-Flow Mechanisms and Alloy Designing. *Materials* **2019**, *12*, 1934. [[CrossRef](#)]
48. Suh, B.-C.; Shim, M.-S.; Shin, K.S.; Kim, N.J. Current issues in magnesium sheet alloys: Where do we go from here? *Scr. Mater.* **2014**, *84–85*, 1–6. [[CrossRef](#)]
49. Mert, F.; Özdemir, A.; Kainer, K.U.; Hort, N. Microstructure and Mechanical Properties of High Pressure Die Cast AM50 Magnesium Alloy Containing Ce. In *Magnesium Technology 2012*; Mathaudhu, S.N., Sillekens, W.H., Neelameggham, N.R., Hort, N., Eds.; Springer International Publishing: Cham, Switzerland, 2016; pp. 149–154.
50. Ahmad, I.R.; Shu, D.W. Compressive properties of AM50 and AZ91D alloys using split Hopkinson pressure bar. In Proceedings of the Second International Conference on Smart Materials and Nanotechnology in Engineering, Weihai, China, 8–11 July 2009; p. 749326.
51. Shan, J. Fracture mechanism of magnesium alloys at room temperature. In Proceedings of the 4th International Conference on Mechatronics, Materials, Chemistry and Computer Engineering 2015, Xi'an, China, 12–13 December 2015; pp. 1109–1114.
52. Dieringa, H.; Fuskova, L.; Fechner, D.; Blawert, C. Mechanical and corrosion behaviour of a hydroxyapatite reinforced magnesium alloy WE43. In Proceedings of the 17th International Conference on Composite Materials, ICCM, Edinburgh, UK, 27–31 July 2009.
53. Lentz, M.; Klaus, M.; Coelho, R.S.; Schaefer, N.; Schmack, F.; Reimers, W.; Clausen, B. Analysis of the Deformation Behavior of Magnesium-Rare Earth Alloys Mg-2 pct Mn-1 pct Rare Earth and Mg-5 pct Y-4 pct Rare Earth by In Situ Energy-Dispersive X-ray Synchrotron Diffraction and Elasto-Plastic Self-Consistent Modeling. *Metall. Mater. Trans. A* **2014**, *45*, 5721–5735. [[CrossRef](#)]
54. Xiong, Y.; Yu, Q.; Jiang, Y. An experimental study of cyclic plastic deformation of extruded ZK60 magnesium alloy under uniaxial loading at room temperature. *Int. J. Plast.* **2014**, *53*, 107–124. [[CrossRef](#)]

Disclaimer/Publisher’s Note: The statements, opinions and data contained in all publications are solely those of the individual author(s) and contributor(s) and not of MDPI and/or the editor(s). MDPI and/or the editor(s) disclaim responsibility for any injury to people or property resulting from any ideas, methods, instructions or products referred to in the content.